Relation between total-column and near-surface NO$_2$ based on in-situ and PANDORA ground-based remote sensing observations

Ying Zhang[a,b], Yuanyuan Wei[c*], Gerrit de Leeuw[a,d], Ouyang Liu[a,b], Yu Chen[e], Yang Lv[a], Yuanxun Zhang[b], Zhengqiang Li[a,b]

[a] *State Key Laboratory of Remote Sensing and Digital Earth, Aerospace Information Research Institute, Chinese Academy of Sciences, Beijing, 100101, China*

[b] *University of Chinese Academy of Sciences, Beijing 100049, China*

[c] *Changcheng Institute of Metrology & Measurement, Beijing, 100095, China*

[d] *R&D Satellite Observations, Royal Netherlands Meteorological Institute (KNMI), 3730AE De Bilt, the Netherlands*

[e] *CMA Public Meteorological Service Centre, Beijing 100081, China*

*Yuanyuan Wei
Corresponding author at the Changcheng Institute of Metrology & Measurement.
Address: Huanshan Village 108, Haidian District, Beijing, China
Postcode：100095
Email：weiyy020@avic.com

Abstract

Nitrogen dioxide (NO_2) is a major pollutant which at high concentrations may affect human health. It is also a photochemically reactive gas which is important for the oxidation potential of the atmosphere and acts as a precursor for the formation of aerosol particles and ozone. However, monitoring of near-surface (NS) NO_2 faces the challenge of spatial discontinuity due to large distances between ground-based monitoring stations, whereas satellite remote sensing provides total vertical column density (VCD) which is related to near-surface (NS) concentrations in a complicated manner. In this study, the relation between total VCD and NS concentrations of NO_2 is analyzed based on total VCD from remote sensing observations using a ground-based Pandora spectrometer and NS NO_2 concentrations from in-situ observations. Both instruments were located at the Beijing-RADI site (Beijing, China) during January 2022. The ratio between total VCD and NS NO_2 concentrations varies throughout the day with substantially different relations in the morning and afternoon. During the night and morning, the atmosphere was vertically stratified, with disconnected layers which prevented vertical mixing of atmospheric constituents. In the afternoon, these layers connected allowing for vertical mixing and transport between the surface and the top of the boundary layer. Thus the prohibition of vertical transport in the morning and the mixing in the afternoon resulted in different relations between the total VCD and NS NO_2 concentrations. These different relationships have consequences for the use of satellite remote sensing to estimate NS NO_2 concentrations.

Keywords: Nitrogen dioxide, remote sensing, air pollution, Beijing, winter

1 Introduction

Nitrogen dioxide (NO_2) can have adverse effects on human health (Eum et al., 2022, 2019; Nordeide Kuiper et al., 2021; Kornartit et al., 2010). NO_2 plays an important role in atmospheric chemistry, and acts as a precursor for the formation of ozone and secondary aerosols in the atmosphere. The major sources of NO_2 are from fossil fuel burning such as power plants, traffic and households. Because of these anthropogenic sources, together with the relatively short atmospheric lifetime of NO_2, high tropospheric NO_2 concentrations are usually observed near highly industrialized regions (van der A et al., 2006), densely populated agglomerations (de Souza et al., 2022) and power plants (Tang et al., 2024), as well as along major highways (Goldberg et al., 2021) and shipping lanes (Ding et al., 2018). In addition, NO_2 is produced from some natural sources such as lightning and soil emissions.

Concentrations of NO_2 in the atmosphere can be measured using satellite-based sensors providing total and tropospheric column densities, ground-based remote sensing using MAX-DOAS or Pandora instruments, or in situ instruments. Satellite remote sensing is currently a widely used technique, for example using the Ozone Monitoring Instrument (OMI, Levelt et al., 2006) on the Aura satellite, and the TROPOspheric Monitoring Instrument (TROPOMI, Veefkind et al., 2012) on the Sentinel-5 Precursor (S5P) satellite. Satellite data show that the total vertical column density (VCD) of NO_2 is highly variable in space and time (e.g., Lamsal et al., 2014; Fan et al., 2021). Duncan et al. (2016) analyzed global NO_2 observed by OMI from 2005-2014 and found that NO_2 levels were initially high over China but had significantly decreased over the Beijing, Shanghai and the Pearl River Delta (PRD) regions in 2014, in response to pollution control measures. In particular, over the PRD region the NO_2 concentrations decreased by about 40%. Also in the following years, the NO_2 concentrations over China have substantially diminished in response to the implementation of emission reduction policy (e.g. van der A et al., 2017; Fan et al., 2021; de Leeuw et al., 2021) and fell below the 2008 level in 2017 (Zhao et al., 2023). However, the decrease seems to have flattened in recent years (Fan et al., 2021).

The Pandonia Global Network (PGN) of Pandora Spectrometer Instruments has been established in 2018 (http://www.pandonia-global-network.org/, last accessed: 10th July 2024) to provide "quality observations of total column and vertically resolved concentrations of a range of trace gases". The PGN data are used, for instance, for the validation of products from environmental satellites. However, the comparison of OMI total VCD of NO_2 with Pandora observations at 6 sites in Korea and the USA by Herman et al. (2019) showed that mean and daily Pandora NO_2 concentrations were 50% or more higher than those retrieved from OMI at sites that were frequently contaminated, such as Seoul, Busan and Washington DC. Tzortziou et al. (2018) reported that Pandora total VCD of NO_2 during the KORUS-AQ coastal cruise experiment (Tzortziou, et al., 2015) were 10-50% higher than OMI-derived total VCD of NO_2. The relationship between total VCD and NS concentrations of NO_2 was complex from the analysis of data from the DISCOVER-AQ campaign in the Baltimore-Washington region in July 2011; the discrepancies were suggested to be caused by the large field of view of OMI (Flynn et al., 2014; Knepp et al., 2015; Reed et al., 2015; Tzortziou et al., 2015). Preliminary validation of total VCD of NO_2 from the Ozone Mapping and Profiler Suite (OMPS) aboard the joint NASA/NOAA Suomi National Polar-orbiting Partnership (Suomi NPP) satellite by Huang et al. (2022) in the USA showed that OMPS total VCD of NO_2 tends to be lower in polluted urban areas and higher in clean areas/events than Pandora observations. Ialongo et al. (2020) and Zhao et al. (2020) obtained similar results from the validation of TROPOMI total VCD of NO_2 using PGN data but the differences were significantly smaller than for the OMI and OMPS data with a coarser spatial resolution than TROPOMI. The validation of TROPOMI total VCD versus Pandora data at the Beijing-RADI site shows the good performance of TROPOMI (Liu et al., 2024). It is noted that Liu et al. re-sampled the TROPOMI data to a spatial resolution of 100×100 m^2, i.e. similar to that of the Pandora observation area.

Satellite-derived total VCD of NO_2 data are often used to determine trends (e.g., van der A et al., 2017; Fan et al., 2021) but, in view of the above, the relation between total VCD and NS concentrations of NO_2 is more complex. For instance, Fan et al.

(2021) discussed the total VCD/NS relationship for selected major urban regions in China during the first 20 weeks after the COVID-19 lockdown and observed substantial differences (their Figure 9). Chang et al. (2022) analyzed data from the Geostationary Environment Monitoring Spectrometer (GEMS) Map of Air Pollution (GMAP) campaign conducted during 2020–2021. Their results indicate that total VCD and NS concentrations of NO_2 exhibit a stronger correlation under advective boundary layer conditions at high wind speeds, where the vertical distribution of NO_2 is more uniform. In contrast, in the presence of plumes from large point sources, either decoupled from the surface or transported from nearby cities, enhance the vertical heterogeneity of NO_2. These plumes contribute to a less consistent relationship between total VCD and NS concentrations of NO_2. Similarly, Liu et al. (2024) show different relations between total VCD and NS concentrations of NO_2 for low and high concentrations which are qualitatively explained in terms of transport and local emissions. Moreover, Thompson et al. (2019), using data from the KORUS-AQ coastal cruise experiment, reported that there is no consistent correlation between total VCD and NS concentrations of NO_2 across different cases and that the relation between total VCD and NS concentrations of NO_2 is complex. Thus, to accurately assess NO_2 pollution in China and effects on air quality, accurate ground-based observations are needed.

Although a large number of ground-based NO_2 observation stations have been established in China since 2012 by the China National Environmental Monitoring Center (CNEMC) of the Ministry of Ecology and Environment of China (MEE) for the provision of the ground-based monitoring data (available at http://www.mee.gov.cn/; last access: 08 July 2024), there are still large areas for which no data are available. Satellite data can fill these gaps by converting satellite observations of aerosols and trace gases from total VCD and NS concentrations. Such data are usually provided from sensors flying on polar-orbiting satellites with global coverage but with a single overpass per day which at most latitudes cannot provide the daily variability of NO_2 characteristics. However, with the launch of geostationary satellites, spatial and temporal distributions of NO_2 concentrations can be obtained within the satellite field

of view throughout the day. The GEO-KOMPSAT-2B geostationary satellite, launched by the National Institute of Environmental Research (NIER) under the Ministry of Environment, Korea, in February 2020, carries the Geostationary Environment Monitoring Spectrometer (GEMS), which provides high-resolution measurements of total VCD of key air quality components (Kim et al., 2020). With the launch of GEMS, the Asian region was the first to achieve coordinated hour-by-hour monitoring of pollutants. GEMS will form a constellation of satellites to monitor air quality globally with high temporal and spatial resolution, together with the Tropospheric Emissions: Monitoring Pollution (TEMPO) mission, launched by NASA on 7 April 2023 to cover the North American region (https://tempo.si.edu/overview.html) and Sentinel-4 planned to be launched on the Meteosat Third Generation Sounder (MTG-S) by the European Organisation for the Exploitation of Meteorological Satellites (EUMETSAT) in 2025 (https://www.eumetsat.int/meteosat-third-generation-sounder-1-and-copernicus-sentinel-4, last visited 18 April 2025).

While geostationary satellites enable continuous daytime observations of total VCD of NO_2, discrepancies between total VCD and NS concentrations of NO_2 concentrations remain a critical challenge. The weak correlation between NS NO_2 concentrations and satellite-derived total VCD of NO_2 (Lamsal et al., 2014) is closely tied to differences in their vertical distribution, atmospheric lifetimes, and chemical reaction pathways (Xing et al., 2017). Despite extensive efforts to derive NS NO_2 concentrations from total VCD measurements (Chang et al., 2025; Wei et al., 2022; Zhang et al., 2022; Dou et al., 2021), the dynamic complexity of the planetary boundary layer introduces substantial uncertainties. Moreover, prior studies have emphasized the roles of vertical NO_2 distribution (Sun et al., 2023; Zhang et al., 2023; Kang et al., 2021) and regional pollutant transport contributions (Yin et al., 2025; Dong et al., 2020; Chang et al., 2019; Li et al., 2017), but research explicitly linking regional transport processes to vertical NO_2 concentration gradients and elucidating their interactive effects remains limited. Song et al. (2024) obtained NS NO_2 concentrations based on the Himawari-8 geostationary satellite using machine learning, which has good performance in the noon

and afternoon, and relatively poor performance in the morning. These knowledge gaps are further exacerbated by satellite data limitations in resolving NS pollution, which has direct implications for human health assessments. To address these challenges, we need to integrate ground-based remote sensing observations with in situ NS NO_2 measurements to investigate vertical decoupling phenomena, and investigate the influence of distinct pollutant transport pathways on NS NO_2 pollution dynamics.

The first operational Pandora instrument in China has been installed at the Beijing-RADI site in 2021, for the ground-based remote sensing of several trace gases, including NO_2. The Beijing-RADI Pandora instrument is part of the PGN network and all data are publicly available via the PGN website (https://data.pandonia-global-network.org/Beijing-RADI/Pandora171s1/, last accessed: 22 Jan 2025) within one day of the observations. The aim of this study is to analyze the relationship between total VCD of NO_2 obtained by remote sensing and NS measurements during a field experiment at the Beijing-RADI site during January 10-29, 2022. In order to better determine and understand the relation between total VCD and NS concentrations of NO_2 concentrations, we also used auxiliary data such as simultaneous measurements of $PM_{2.5}$ mass concentrations, lidar observations, meteorological parameters, and satellite observations. Section 2 presents the experiments and data, Section 3 presents the main results, and the conclusions and discussion are presented in Section 4.

2 Materials and Method

2.1 Site description

Beijing is a metropolis with an area of 16,800 square kilometers and a population of nearly 22 million (2023) (https://worldpopulationreview.com/world-cities/beijing-population, last accessed: 22 Jan 2025). High mountains are located to the north and west of Beijing (Fig. 1). The rapid economic development of Beijing and the topography of the area lead to emission of pollutants which may either disperse or accumulate, depending on wind direction and wind speed. During northwesterly winds, clean air is transported from the mountains, whereas during southerly winds polluted

189 air is transported from the highly industrialized North China Plain. The southerly
190 airflow is blocked by the mountains to the west and north and thus pollution
191 accumulates, in particular during certain weather conditions conducive for the
192 formation of smog, such as low wind speed. Photochemical processes may further
193 contribute to the build-up of pollution which may result in the formation of haze.

194   The Beijing_RADI site is located at the roof (22 m above the surface) of the
195 Aerospace Information Research institute of the Chinese Academy of Sciences (40.004°
196 N, 116.379° E, elevation 59 m), which in turn is located in the north of Beijing between
197 the Fourth and Fifth Ring Roads at the edge of the Olympic Parc. The site is
198 representative for an urban background affected by vehicle exhaust, combustion and
199 domestic emissions including those from heating during wintertime.
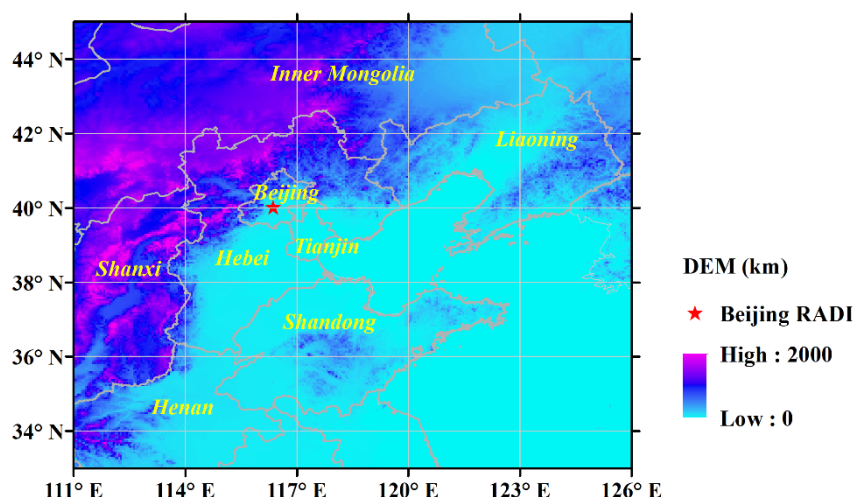
200

Figure 1. Digital elevation map of the study area showing the location of the Beijing-
RADI site (40.004° N, 116.379° E, altitude at 59 m) (red star) and surrounding
mountains.

204 A short-term field experiment was carried out at the Beijing-RADI long-term
205 observation site during January 10-29, 2022. Pandora provided total VCD of NO_2
206 concentrations in 4 layers, information on the spatial distribution of total VCD of NO_2
207 was obtained from TROPOMI and a lidar provided aerosol backscatter profiles showing
208 the vertical structure and evolution of the atmospheric boundary layer. The NS
209 parameters were measured with instrumentation mounted near the Pandora on the roof

210 of the AirCAS building, as described in the following sections.

2.2 Observations of Column-Integrated Parameters and Vertical Profiles

2.2.1 Pandora

Pandora is a UV-visible spectrometer which can provide high-quality measurements of spectrally resolved direct-sun/lunar or sky scan radiances. It uses direct solar measurements to obtain total VCD of NO_2, and sky measurements to obtain the vertical layer concentrations of NO_2, with a FOV of 2.6° in direct sun mode and 1.5° in sky mode (Cede, 2024). Based on the Beer-Bouguer-Lambert law, the spectra observed at 400~470 nm in direct-sun mode are used to invert total VCD of NO_2 using the differential optical absorption spectroscopy (DOAS) technique of trace gas spectral fitting. Pandora's direct sun measurements depend only on the geographic location with a known solar zenith angle which simplifies the air mass factor for correction of the atmospheric light path (Chang et al., 2022). Pandora measures total VCD of NO_2 with a clear-sky precision of 0.01 DU and a nominal accuracy of 0.1 DU (Herman et al., 2009). In view of this high precision, we use total VCD of NO_2 from the nvs3 product in this study and select data with quality control flag of L10. Diffuse (scattered) radiation is measured at 5 pointing zenith angles (PZAs) in sky mode which, together with the direct sun measurement, provides information on the tropospheric VCD and on the surface concentrations. The PZAs are 0°, 60°, 75°, 88° and a maximum angle taken as 89°. The measurements are taken in a V shape (all angles are measured twice around a central angle) as described in Cede (2024). Four partial columns of NO_2 concentrations are provided by the PANDORA inversion. The first step is the estimation of the effective height corresponding to a given PZA, and then calculate differential air mass factors for the NO_2 and the air-gas for each layer. The profile shape of the partial columns is determined as a variation of the air-gas shape. The average number density of the NO_2 in each layer is then calculated. The partial column amounts can be obtained from the concentrations multiplied with the layer width as described in the Manual for Blick Software Suite (Cede, 2024), Section 6.7. The NO_2 of the partial column can be obtained from the uvh3 product which was downloaded from the PGN website

239 (https://pandonia-global-network.org, last accessed: 22 Jan 2025). We converted these

240 partial column concentrations into layer-averaged volume mixing ratios and

241 interpolated them to 6 standard levels (0.2, 0.5, 1.0, 1.5, 2.0, 2.5 km) for visualization.

2.2.2 Lidar

243 A small lidar developed by the Hefei Institute of Physical Sciences, Chinese

244 Academy of Sciences, was used for continuous measurements of aerosol backscatter

245 profiles during day and night. The GBQ L-01 aerosol lidar consists of a laser, optical

246 unit, control unit board, high-speed signal acquisition card, industrial motherboard and

247 communication module. The GBQ L-01 aerosol lidar uses a high-frequency pulse laser

248 emitting linearly polarized light at a wavelength of 1064nm. The optical unit consists

249 of a transmitter and a receiver. The optical transmitter unit emits laser light pulses,

250 which are expanded before they are emitted into the atmosphere. The optical receiver

251 unit consists of a telescope which focuses the back-scattered light onto an optical

252 detector which in turn is connected to an amplifier unit. The vertical and parallel

253 polarized components of the back-scattered light are separated by the polarizing prism

254 in the receiving channel. The industrial motherboard carries lidar acquisition and

255 control software and data analysis software to control the overall operation of the

256 system.

2.2.3 TROPOMI

258 The TROPOMI (TROPOspheric Monitoring Instrument) is a passive-sensing

259 hyperspectral nadir-viewing imager aboard the Sentinel-5 Precursor (S5P) satellite,

260 launched on 13 October 2017. S5P flies at an altitude of 817 km in a near-polar sun-

261 synchronous orbit. The local equator overpass time in the ascending node is 13:30, and

262 the repetition period is 17 days (KNMI, 2017). TROPOMI's four separate

263 spectrometers cover wavelengths in the ultraviolet (UV), UV–visible (UV-VIS), near-

264 infrared (NIR) and short wavelength infrared (SWIR) spectral bands (Veefkind et al.,

265 2012). The NO_2 used in this study is derived from spectral measurements of solar

266 radiation in TROPOMI's UV–VIS wavelength bands (van Geffen et al., 2015, 2019).

267 Compared to the relatively small field-of-view of the Pandora instrument, the size of

the TROPOMI ground pixel (3.5 km $\times$ 5.5 km; across $\times$ along track) is relatively large. In addition, only tropospheric vertical column densities (VCDs) for NO_2 were available during the time period of this study. The TROPOMI tropospheric VCDs for NO_2 are only used as a qualitative reference for upwind concentrations for the evaluation of effects of long-range transport using air mass backward trajectories and not for quantitative analysis. Furthermore, tropospheric NO_2 column densities are used because these are more representative of near-surface NO_2.

2.3 Near Surface Measurement

2.3.1 Trace Gas Analyzer

The Thermo Fisher Scientific Model 42i Trace Level Chemiluminescence NO-NO_2-NO_x Analyzer was used to measure NS NO_2 concentrations. This instrument first transforms NO_2 into nitric oxide (NO) using a molybdenum NO_2 to NO converter heated to about 325 °C. Then, NO and ozone (O_3) react to produce a characteristic luminescence with an intensity linearly proportional to the NO concentration (Model 42i Trace Level Manual, 2007). NO_2 values are derived by subtracting NO from NO_x measurements. Measurements were made every minute during the observation period.

2.3.2 Beta attenuation monitor

Ground-based near-surface $PM_{2.5}$ concentrations were measured using the beta attenuation monitor Met One BAM-1020 (BAM 1020 particulate monitor operation manual) equipped with a $PM_{2.5}$ inlet. The Met One BAM-1020 collects aerosol particles on glass filter tape. $PM_{2.5}$ is measured using beta rays generated by a small ^{14}C source (https://metone.com/products/bam-1020/). At the start of every measurement cycle, the flux of beta rays is measured across clean filter tape, to determine a zero reading. Next, the filter tape is advanced and ambient air is sampled at the same spot, with a controlled air flow, thereby impregnating the tape with $PM_{2.5}$. After the sampling is completed, the tape retracts and $PM_{2.5}$ samples are dried (in an environment with relative humidity lower than 40% which removes most of the water content) by a built-in heater. Then the concentration of $PM_{2.5}$ collected on the filter tape is measured as described above. Samples are taken every hour.

2.3.3 Auxiliary meteorological data

In addition to the above observations, we also use weather maps, meteorological surface observations and sounding observations published by the World Meteorological Organization (WMO) to aid in our analyses. Weather maps for the Asian region are published by the Korea Meteorological Administration and can be downloaded at http://222.195.136.24/chart/kma/data_keep (last accessed: 22 Jan 2025). We downloaded the surface and sounding observations of meteorological station 54511 in Beijing, located at 39.93N, 116.28E, which is part of the WMO network. These data are available from the website of the University of Wyoming (http://weather.uwyo.edu/surface/) (last accessed: 22 Jan 2025). Although this station is far away from our experimental site (about 23 km), it is representative of the macroscopic changes of the meteorological conditions in Beijing.

2.4 HYSPLIT Model

To better understand the regional transport pathways and source regions at different altitudes, backward trajectories from the Hybrid Single Particle Lagrangian Integrated Trajectory (HYSPLIT; Draxler & Hess, 1998) model were used. The HYSPLIT model assumes that the parcel trajectory is formed through time integration and spatial differences when moving in the wind field. The path of the air mass is mainly related to the air flow situation, pressure system movement and topography (Draxler & Hess, 1998). The HYSPLIT model has the ability to deal with a variety of meteorological input fields and physical processes, and can also be used to describe atmospheric transport, diffusion and deposition of pollutants and harmful substances (Stein et al., 2015). In this study, the backward trajectories were initialized for arrival at the Beijing-RADI site at 300 m, 500 m, and 1000 m. The HYSPLIT model was run at https://www.ready.noaa.gov/HYSPLIT_traj.php, with the input meteorological field data ($0.25° \times 0.25°$) provided by the Global Forecasting System.

3 Results and Analysis

3.1 Data overview

Time series of the measured NS and total VCD of NO_2 during the study period are presented in Fig. 2a. For comparison of NS NO_2 concentrations with Pandora observations, they are expressed in mg m^{-3}. Fig 2a shows the common diurnal variation of the NO_2 concentrations, i.e. a gradual decrease in the morning to a minimum around mid-day, followed by a gradual increase in the afternoon to a maximum value during the night. This diurnal variation is due to photochemical reactions during daytime, meteorological effects and anthropogenic emissions during certain hours (for instance during rush hour) (e.g., Atkinson, 2000; Boersma et al., 2009; Zhang et al., 2016; Cheng et al., 2018; Li et al., 2021). Total VCD of NO_2 concentrations can only be measured with Pandora during day time. The diurnal variations between 8:00 and 16:00 local Beijing time (UTC+8; throughout this paper local time, LT, will be used) at the Beijing-RADI side are similar to those of NS NO_2. Based on the variation of the NS NO_2 concentrations (Fig. 2a) three periods are considered during the study period: Period I: 10 to 18 January, with strong diurnal variations and high NO_2 concentration peaks; Period II: 19 to 24 January, NS NO_2 sharply decreases and then increases with stronger fluctuations, but total VCD of NO_2 are not available due to the presence of clouds; Period III: 25 to 30 January, a sudden drop occurred on January 25, and low NO_2 concentrations with some narrow peaks lasted until the 30th.

The time series of the NS PM$_{2.5}$ concentrations in Fig. 2b shows four peaks in Period I, with maximum values during the night and very low concentrations (<10 μg m^{-3}) during daytime. The maxima were relatively low on 12 and 17 January (~25 μg m^{-3}), whereas on 14 and 18 January the PM$_{2.5}$ peak concentrations were ~120 and ~70 μg m^{-3}. During Period II, the PM$_{2.5}$ concentration increased steadily from less than 25 μg m^{-3} on 20 January to more than 125 μg m^{-3} on the 24th, with similar day/night variations as in Period I. During Period III, the PM$_{2.5}$ concentrations were relatively low (<25 μg m^{-3}) and there was no clear diurnal variation.

351   The air temperature and relative humidity (RH) during the study period are

352   presented in Fig. 2c and the wind speed and wind direction are presented in Fig. 2d.

353   During Period I, air temperature, RH and wind speed all varied strongly with a clear

354   diurnal pattern: elevated wind speed during the day, with daily maxima between about

355   7 and 13 m s^{-1}, and very low wind speed during the night ($<$2 m s^{-1}); day time air

356   temperatures around 0°C and night time temperatures around -10°C; dry air during the

357   day (RH~20%) and more humid during the night (RH of 60-80%). The wind was mostly

358   from northerly directions (NW-NE) and veering during the night. During Period II, the

359   air temperature increased gradually from about -5°C to about 0°C, with small diurnal

360   variations, and RH increased initially from 40% to 60% on 20 January and then

361   gradually to about 70%, with little day/night variations. During the nights of 22-25

362   January the humidity was very high, the RH sensor saturated and reported maxima close

363   to 100%. Wind speed during this period was low ($<$ 3 m s^{-1}) and wind direction was

364   mostly SE. During period III, day/night temperature and RH fluctuations occurred, with

365   day time air temperatures above 0°C and gradually rising and RH varying between 20%

366   during the day and 60% during the night. Wind speeds were higher during the day,

367   mostly a little higher than 3 m s^{-1}, than during the night (close to 0 m s^{-1}) and wind

368   direction was mostly northerly.

369   The variations of the NO$_2$ and PM$_{2.5}$ concentrations were similar in the sense that

370   the minimum and maximum peak concentrations occurred at about the same time, but

371   with differences in the ratios between minima and maxima. The occurrence of peak

372   concentrations during the night is consistent with the variation in meteorological

373   conditions, with maxima during low wind speed and low air temperature, conducive for

374   the formation of a nocturnal boundary layer in which the concentrations accumulate

375   near the surface. This is observed during Periods I and III. During Period II, however,

376   there were no Pandora observations during day time due the occurrence of clouds. This

377   suggests that clouds may also have been present during the night. Hence radiative

378   cooling was reduced and air temperature did not decrease as much as during the other

379   periods. Wind speed was low, thus pollutants were not transported away and

14

380 accumulated in the area, as also indicated by the high RH. Hence the concentrations of

381 NO_2 and $PM_{2.5}$, as well as RH, gradually increased during period II, with relatively

382 small diurnal variations.

383   For further analysis, we selected two cases for which both total VCD and NS

384 concentrations of NO_2 data were available, including lidar observations and air mass

385 trajectories. The selected cases are the periods when both NO_2 and $PM_{2.5}$ concentrations

386 were high, i.e. on 14 and 18 January, when the 24-hour average NO_2 concentrations

387 exceeded 80 mg m^{-3}. The first pollution episode (case 1) started in the afternoon of

388 January 14 and ended in the morning of January 15. The other pollution episode with

389 high NS NO_2 occurred on January 18 (case 2). The diurnal variation of the NS NO_2

390 concentrations was similar in both cases, while the air temperature, RH, wind speed

391 and wind direction show that also the meteorological situations were similar. However,

392 differences are observed in the temporal variations of total VCD of NO_2 concentrations

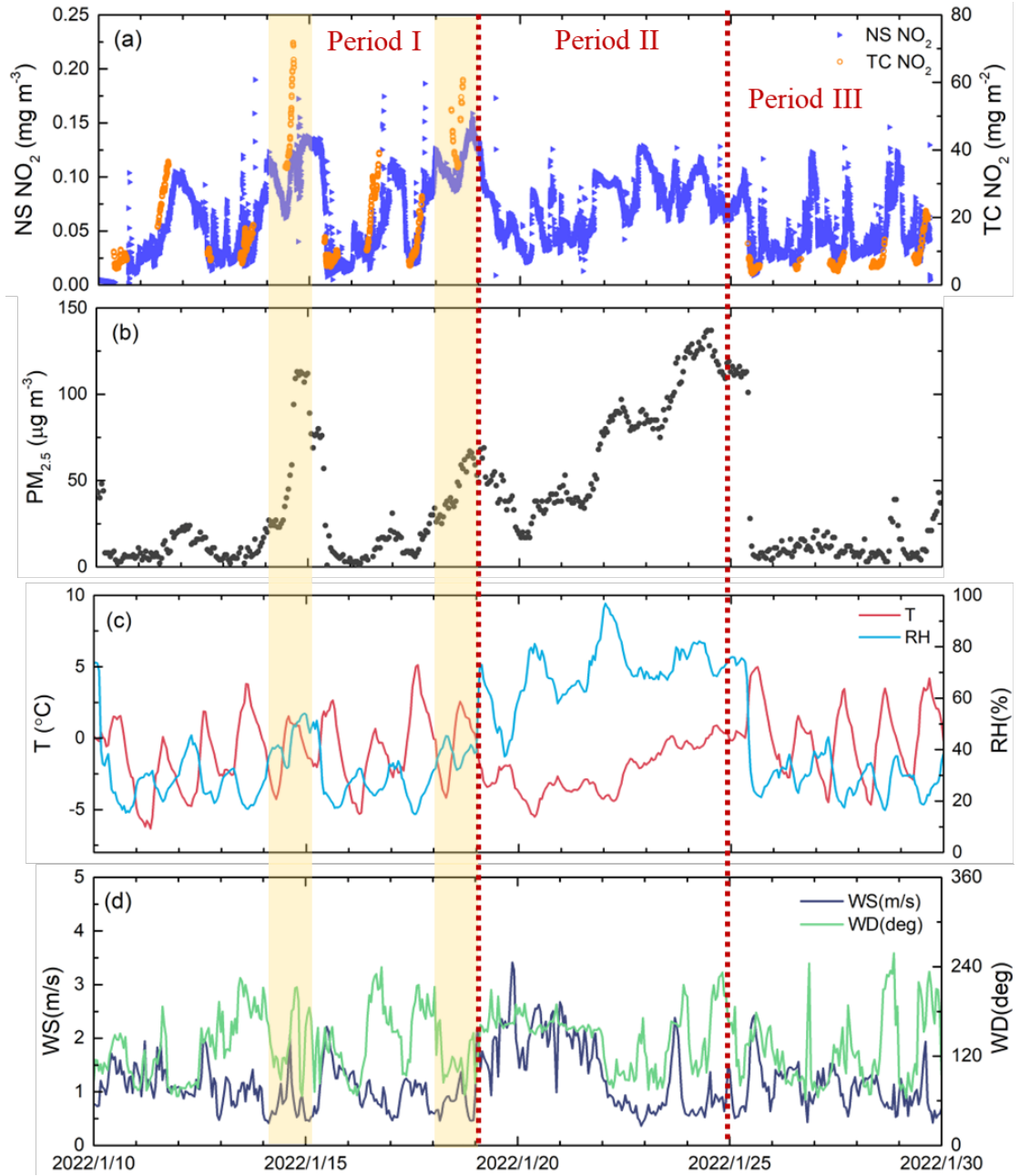393 versus NS NO_2 concentrations and in $PM_{2.5}$ concentrations.

Figure 2. Time series of observed parameters from Jan 10 to 29, 2022 (a) total VCD and NS concentrations of NO_2 concentrations, (b) NS $PM_{2.5}$ concentration, (c) temperature and related humidity, and (d) wind speed and wind direction from WMO meteorological station 54511 in Beijing. The vertical dotted lines mark the boundaries between the three periods and the yellow shaded rectangles mark the two cases discussed in Section 3.2.

3.2 Variations of total VCD and NS concentrations of NO$_2$ during the two selected cases

Many studies (Yin et al., 2025; Dong et al., 2020; Chang et al., 2019; Li et al., 2017) indicated that the pollution in Beijing mainly originates from three pollution transport patterns: southwest (SW), southeast (SE), and south mixing (SM) patterns. Among them, the most representative are the SW transport path from Shanxi province to Shijiazhuang-Baoding-Beijing and the SE transport path from Shandong province to Cangzhou-Langfang-Tianjin-Beijing. However, few studies have explored the vertical transport of pollution types. Cases 1 and 2 are representative for the widespread SW and SE patterns, respectively. The processes influencing the concentrations are identified based on lidar data, providing information on the boundary layer structure, together with large scale weather maps and air mass trajectory analyses, providing information on sources of pollutants and their transport over a wider area. Our study primarily focuses on the correlation between total VCD and NS concentrations of NO$_2$. Total VCD of NO$_2$ are provided by the passive remote sensing instrument PANDORA, which does not provide reliable observations on cloudy days, as mentioned above. This is the reason why we only selected cases during Period I and did not obtain cases during Period II, when pollution was more severe.

3.2.1 Case 1: Disconnected boundary layers merging (14 January, 2022)

Time series of the total VCD and NS concentrations of NO$_2$ on 14 January 2022 (Fig. 3a) show their different evolution throughout the day. NS concentrations showed diurnal variation, decreasing from midnight (0.11 mg m^{-3}) to morning (0.065 mg m^{-3} at 10:30), followed by an afternoon increase and strong evening fluctuations (0.04-0.175 mg m^{-3}) likely associated with rush hour emissions and domestic heating. During the limited observation window (10:30-15:30) for Pandora, both VCD and NS concentrations initially showed similar behavior with minimal variation. However, their temporal patterns diverged after 13:00 while NS concentrations plateaued, VCD exhibited rapid growth (40 to 72 mg m^{-2} between 12:00-15:00), nearly doubling before declining slightly. The difference in the temporal behavior between the total VCD and

430 NS concentrations of NO_2 is amplified in Fig 3b which shows a scatterplot between the

431 total VCD and NS concentrations. Observations before and after 13:00 are plotted with

432 different symbols and color coded in blue and red, respectively. For each of these two

433 data sets, before and after 13:00, TS and NS concentrations are well correlated with

434 linear correlation coefficients R of 0.94 and 0.85, respectively, but with significantly

435 different slopes.

436   The different behavior of the total VCD and NS concentrations of NO_2 can be

437 explained by considering the dynamical behavior of the boundary layer structure. Lidar

438 observations reveal the vertical structure of the atmospheric boundary layer from the

439 variation of the lidar signal as a function of height. A 3-D plot of the vertical variation

440 of the lidar signal, measured on 14 January 2022 at the Beijing-RADI site, close to the

441 Pandora and the ground-based measurements, is presented in Fig. 3c. The lidar signals

442 are color-coded according to the scale to the right of Fig. 3c and each vertical line shows

443 the variation of the lidar signal with height, plotted along the primary vertical axis. The

444 time of measurement of each profile is plotted along the horizontal axis. The lidar signal

445 in this figure is range-corrected, i.e. corrected for attenuation as the laser light

446 propagates in the atmosphere away from the emitter and, after backscattering by aerosol

447 particles, back to the receiver. The time between emission of the laser pulse and

448 receiving the backscattered signal is a measure for the height where the backscattering

449 takes place (after correction of the slant to a vertical optical path) and the intensity is a

450 measure for the aerosol concentration.

451 The lidar observations in Fig. 3c revealed a complex boundary layer structure with

452 distinct aerosol layers. The data show a well-mixed shallow boundary layer between

453 midnight and 03:00 and the formation of an internal boundary layer after about 04:00,

454 disconnected from the layer above. The internal boundary layer rises gradually until

455 about 11:00 (up to about 400 m), with the clean layer above (between 400 and 500 m),

456 and a new layer (at heights of approximately 800 to 900 m) appears around 07:00,

457 probably due to advection. This vertical variation indicates a disconnected boundary

458 structure with two disconnected layers, likely caused by nocturnal cooling (Stull, 1988).

459   The temperature gradient prohibited material exchange between these layers, leading

460   to the accumulation of near-surface emissions and the trapping of trace gases and

461   aerosols in the upper layer. The occurrence of such a situation is consistent with the

462   observations discussed in Section 3.1 and Fig. 2, with low wind speed, lowest air

463   temperature during period I (-12°C) and enhanced RH (indicating trapping of water

464   vapor together with decreased air temperature). Note that wind direction was south-

465   easterly during a short period of time on 14 January with a wind speed of 2 m s^{-1},

466   slightly more than during the rest of the day when the wind direction was northerly.

467   During south-easterly winds, polluted air may be advected to the Beijing-RADI site,

468   whereas during northerly wind clean air is advected (Liu et al, 2024).

469   The lidar data in Fig. 3c show that after 12:00, the lower layer deepened and backscatter

470   was observed from the clean layer indicating that aerosol is gradually mixed into that

471   layer which completely disappears around 14:00. At the same time, the lidar signal from

472   the growing lower layer increased gradually whereas after 13:00 the lidar signal from

473   the upper layer became smaller, indicating that the aerosol concentration decreased until

474   both layers were mixed around 14:00 into a well-mixed boundary layer. After 15:00,

475   the lidar signal increased, first near the surface and then growing throughout the

476   boundary layer. The increase of the NS concentrations (Fig. 3a) is consistent with the

477   highest $PM_{2.5}$ concentrations as presented in Fig. 2b and the overall increase of the lidar

478   signal, indicating increasing aerosol concentrations. This is confirmed by AERONET

479   AOD observations at the Beijing-RADI site (https://aeronet.gsfc.nasa.gov/cgi-

480   bin/data_display_aod_v3?site=Beijing_RADI&nachal=2&level=2&place_code=10)

481   which however were only available until 16:00 LT.

482   The vertical variation of the NO_2 concentrations, derived from the Pandora sky

483   radiance measurements at four elevations, is presented in Fig. 3d. Pandora data are only

484   available during day time and therefore only the period from 08:00-16:30 can be shown.

485   The NO_2 concentrations are available in 4 layers. Assuming that NO_2 is uniformly

486   distributed within each layer, the data were interpolated to form a time series of NO_2

487   vertical distributions, similar to the lidar profiles. The data in Fig. 3d show the similar

488 behavior of the NO_2 concentrations and the aerosol backscatter, with increasing

489 concentrations between 12:00 and 17:00 and their vertical mixing. In particular the

490 increase around 15:00 is evident in both the Pandora and lidar observations. However,

491 the Pandora observations do not show the occurrence of disconnected boundary layers

492 in the morning. Instead, the Pandora observations show an enhanced layer between 300-

493 800 m, rather than the more detailed structure visible in the lidar data. These differences

494 stem from the difference in vertical resolution between the PANDORA and the lidar:

495 the total VCD from PANDORA is divided into two layers (approximately 300-800 m

496 and 800-1700 m) within the detailed stratified height range (300-1000 m) observed by

497 lidar. Consequently, the fine stratified structure within 1000 m cannot be identified with

498 the available PANDORA data.

499   The overall similarity between the variations in the lidar and Pandora observations

500 supports the use of lidar observations to explain the dynamic behavior of the NO_2

501 concentrations. In particular, the different relations between total VCD and NS

502 observations before and after 13:00 (Fig. 3b), can be explained by the occurrence of

503 disconnected layers. The variations of the NS NO_2 concentrations until 13:00 reflect

504 the effects of chemical processes and emissions within the atmospheric layer near the

505 surface and within the elevated layer where only removal processes influence the NO_2

506 concentrations. As a result, the temporal variation of the concentrations in both layers

507 was in part influenced by the same processes, differences were not large (Fig. 3a) and

508 the relationship between the total VCD and NS concentrations was linear with a small

509 slope (174.24) and well-correlated (R=0.94) (Fig. 3b). In the afternoon, such processes

510 resulted in the increase of NO_2 concentrations, but when the two layers connected and

511 the wind speed increased somewhat (Fig 2c, d) NO_2 was mixed throughout the whole

512 boundary layer up to about 1000 m. Hence the usual afternoon increase of NO_2

513 concentrations near the surface (Liu et al., 2024) was offset by upward transport,

514 distributing the NO_2 across the whole boundary layer and thus enhancing the total VCD.

515 This well illustrated by the time series of both NC and total VCD between 13:00 and

516 15:00 (see Fig. 3a). As a result, the relationship between total VCD and NS changed

substantially after 13:00 (Fig. 3b).
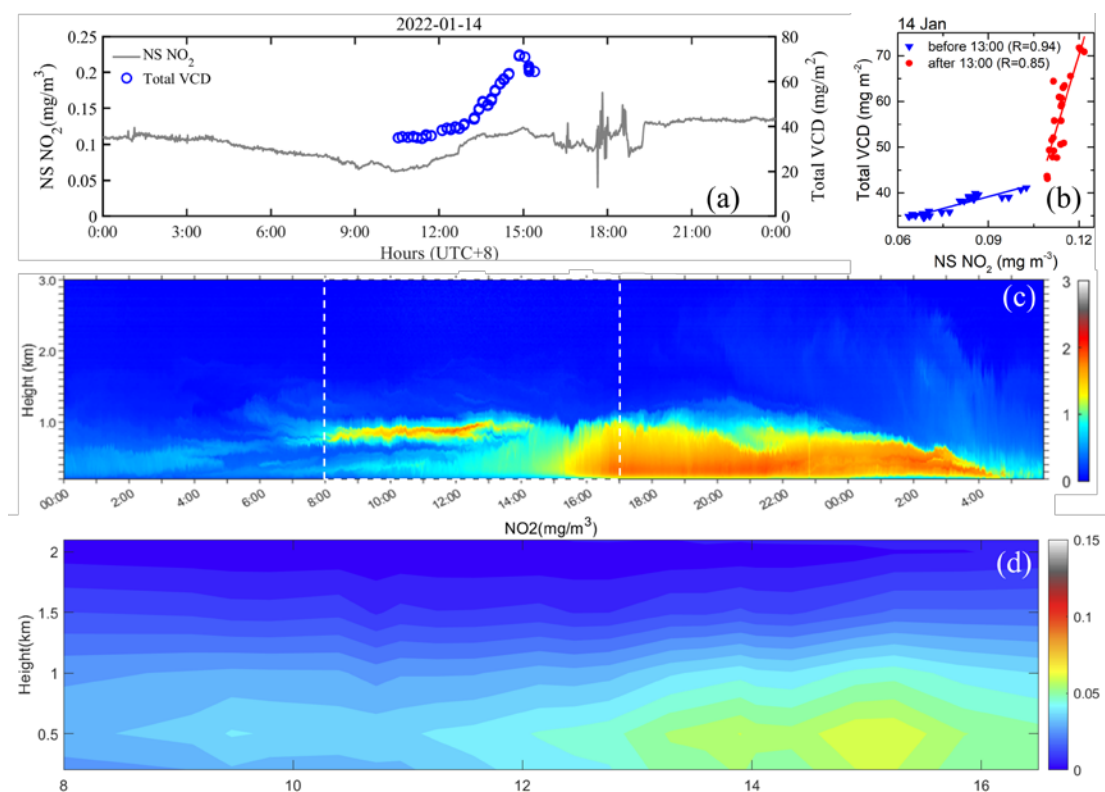
Figure 3. (a) Time series of NS NO$_2$ (grey line) and total VCD of NO$_2$ (blue circles) at the Beijing RADI site (40.004°N, 116.379°E) on Jan 14, 2022; (b) scatterplots of total VCD and NS concentrations of NO$_2$ and fits to these data during the morning (before 13:00) and during the afternoon (after 13:00), showing different relationships as discussed in the text; (c) time series of vertical profiles of range-corrected lidar signal at 1064 nm. Note that the lowest height in Fig. 3c is 100 m; (d) time series of NO$_2$ vertical profiles derived from Pandora sky radiance measurements. Note that the Pandora profiles are constructed from layer-averaged volume mixing ratios interpolated to 6 standard levels and the lowest level is 0.2 km.

The effect of transport on the NO$_2$ concentrations at the Beijing-RADI site on 14 January 2022 was analyzed using the data presented in Fig. 4: the spatial distribution of tropospheric NO$_2$ columns derived from TROPOMI data (overpass time 13:30), the synoptic weather map at 00 UTC and 24-hour backward trajectories for arrival at the Beijing-RADI site at altitudes of 300 m, 500 m and 1000 m, at 10:00, 13:00 and 16:00 LT. The TROPOMI data show the relatively high tropospheric NO$_2$ concentrations over

534   the study area, in particular over an elongated area stretching from the SW to the NE

535   over Hebei Province, including Beijing (compare with Fig. 1), and from Beijing

536   eastward. This area is bounded by the Taihang mountains in the west and by the Yan

537   mountains in the north, blocking transport of pollutants. The weather map in Fig. 4b

538   shows the pressure distribution and location of low pressure areas resulting in wind

539   from the SW, i.e. along the direction of the elongated area with elevated NO_2

540   concentrations (see Fig. 4a). This is confirmed by the air mass trajectories in Fig. 4c,

541   all showing overall transport from the SW. However, the trajectories arriving at 10:00

542   LT show that during the last 8h, the air mass arriving at 300 m came from the NE at

543   low wind speed and the airmass arriving at 500m came from the NW at even lower

544   windspeed. The airmass arriving at 1000 m came from the SW during the last 14 h

545   before arrival and from the NW during the earlier 12 hours. The airmasses arriving at

546   13:00 show similar trajectories. These trajectories are consistent with the lidar

547   observation of disconnected layers, with different air mass trajectories during the last

548   hours before arriving at the Beijing-RADI site and thus possibly different composition.

549   The air mass arriving at 1000 m had been at high elevations during its entire 24 h

550   trajectory and originated from higher than 1500m, but those arriving at 300 and 500 m

551   originated from the surface at different locations separated by tens of km and may thus
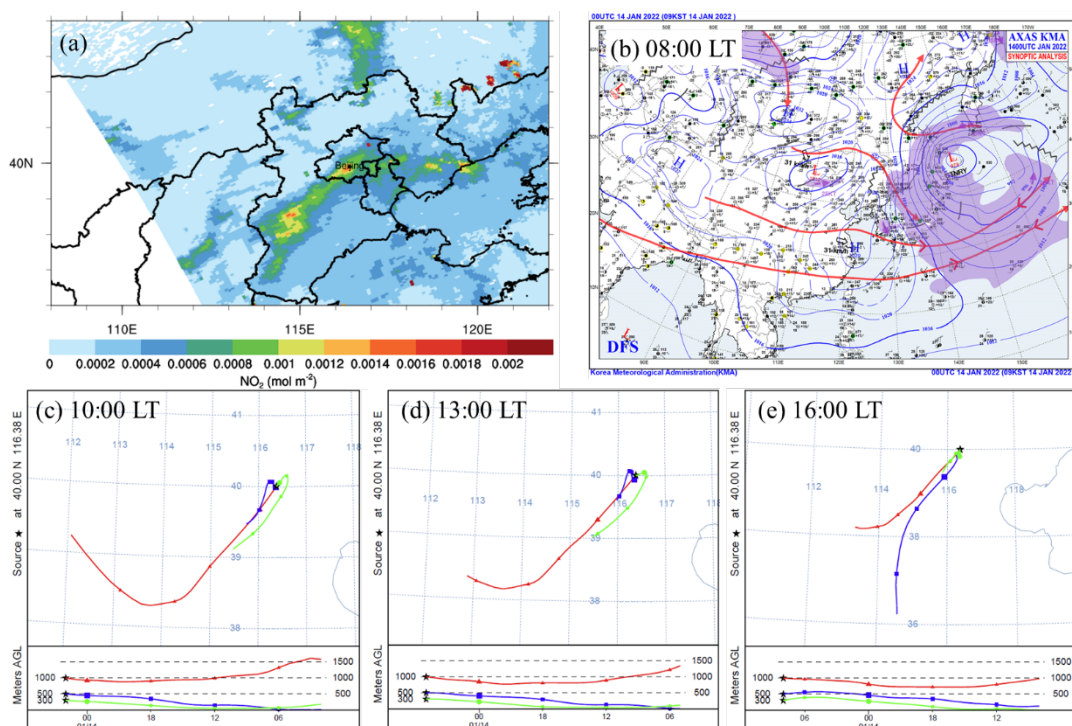
552   have been influenced by different sources.

Figure 4. (a) Spatial distribution of tropospheric NO_2 in the study area derived from TROPOMI data on 14 January 2022; (b) Synoptic weather map at 00:00 UTC (08:00 LT); (c-d) 24-hour backward air mass trajectories arriving at the Beijing-RADI site at 10:00 (c), 13:00 (d) and16:00 LT (e), at heights of 300, 100 and 1000 m, calculated using the HYSPLIT model with 6h time steps (00, 06, 12 and 18) and a shorter time step to the arrival time.

3.2.2 Case 2: Multi-layer structure on 18 January, 2022

Time series of the total VCD and NS concentrations of NO_2 on 18 January 2022 are shown in Fig. 5a, together with a scatterplot between the total VCD and NS concentrations in Fig. 5b and 3-D plots of the vertical variation of lidar backscatter coefficients in Fig. 5c and Pandora-derived NO_2 concentrations in Fig. 5d. The observational data for 18 January reveal distinct diurnal patterns in NO_2 dynamics, with NS concentrations exhibiting higher baseline levels than on 14 January while following a similar initial decreasing trend until 11:30. Subsequently, NS concentrations demonstrated nonlinear growth, plateauing at 0.12 mg m^{-3} (about 1 hour after 14:30) before further increasing to 0.16 mg m^{-3} by 21:00, attributed to combined rush-hour emissions and reduced photochemical dissipation. Concurrently, total vertical column

23

density (VCD) displayed accelerated morning depletion (from 54 to 36 mg m^{-2} between 08:30 and 12:30), but in contrast to the 14th, after 11:30 the total VCD of NO$_2$ concentrations continued to decrease while the NS NO$_2$ concentrations increased. Hence, in this situation, it may be difficult to determine NS NO$_2$ concentrations from the relationship (R=0.40) before 13:00 (Fig 5b). After 13:00, the total VCD of NO$_2$ increased from about 37 mg m^{-2} to almost 60 mg m^{-2} at 16:30, with a plateau around 15:00, and the scatterplot in Fig. 5b shows a good correlation between TS and NS NO$_2$ concentrations.

The lidar data in Fig. 5c, with lower intensity than on 14 January, indicate smaller aerosol concentrations on 18 January than on 14 January, consistent with the smaller PM$_{2.5}$ concentrations (in Fig. 2b). The lidar data show the occurrence of multiple layers during the night and morning, with sharp boundaries indicating that aerosol particles are trapped in rather shallow layers with little or no exchange between these layers. After 10:30, the boundaries between layers became less sharp, indicating the onset of vertical transport, although the very shallow clear layer (dark blue) between 500 and 600 m indicates a clear separation between the lower and upper layers, prohibiting vertical transport. Around 13:00 this shallow layer disappeared and after 15:00 the atmospheric boundary layer appeared well-mixed up to the top at about 800m.

The time series of the NO$_2$ vertical distributions in Fig. 5d shows that NO$_2$ concentrations were lower on the 18th than on the 14th, and concentrated below 1000 m. The observation of lower concentrations on the 18th and the 14th seem to be in contrast with the higher NS concentrations on the 18th than on the 14th mentioned above. However, the Pandora profiles are constructed from layer-averaged volume mixing ratios interpolated to 6 standard levels and the lowest level is 0.2 km. Hence, in view of the layered structure on the 18th, the higher NS concentrations may be disconnected from the lowest layer set at 0.2 km. It is further noted that the Pandora vertical distributions show lower NO$_2$ concentrations on the 14th than on the 18th in the morning, whereas they are higher in the afternoon of the 14th. The NO$_2$ concentrations and their vertical distributions varied between 08:00 and 12:30, with an initial increase between

08:00 and 10:00 with a broad elevated maximum centered around 500 m and another small maximum around 11:00. Apart from these, the NO_2 concentrations were rather homogeneously distributed up to the top of the atmospheric boundary layer at about 800 m as also indicated by the lidar data. After about 12:00 the NO_2 concentrations increased with a significant enhancement after 14:00.

The evolution of the atmospheric boundary layer, as shown in detail by the lidar data, and the variation of the NO_2 concentration profiles provide a plausible explanation for the evolution of the total VCD and NS concentrations of NO_2 and their ratios, with changes around 11:30 and 13:00. The plateau in the NS NO_2 concentrations may be indicative of the dilution near the surface due to upward transport and vertical mixing, at the same time increasing the TS NO_2 concentrations.
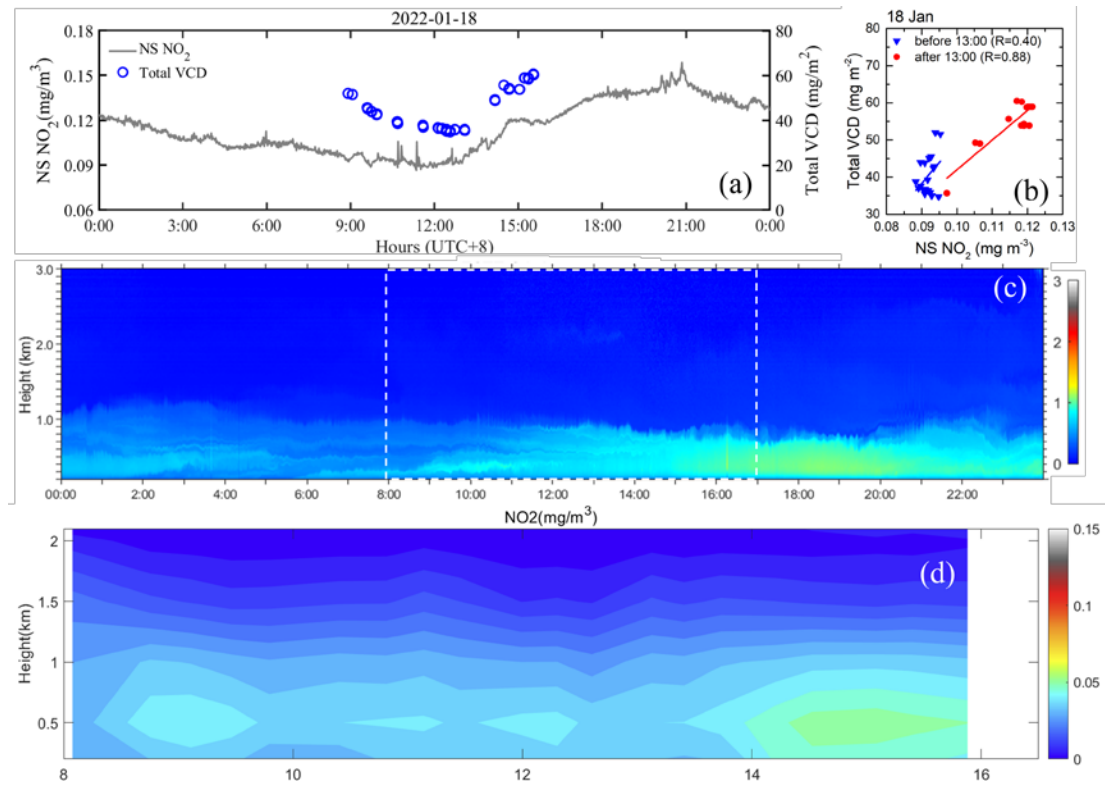
Figure 5. Same as Fig. 3 but for 18 January, 2022.

Fig. 6 shows the large scale situation for the study area on 18 January. The TROPOMI data in Fig. 6a show the spatial distribution of the tropospheric NO_2 VCDs which are highest to the SE of Beijing, in Hebei/Tianjin and over the Yellow Sea. Over Beijing, the tropospheric NO_2 VCDs, as indicated by TROPOMI, are substantially lower than

in case 1. This can be explained by the transport from clean areas to the west and west-north-west of Beijing, as indicated by the air mass trajectories arriving in Beijing at 300m, 500 m and 1000m, at 10:00, 13:00 and 16:00 LT (Fig. 6c). The trajectories of the air masses arriving at 10:00 LT show a clear difference between the lower and higher layers visible in the lidar data: where the air arriving at 1000 m originated from the WNW and had traveled during the last 24 h over clean areas (Fig. 6a) over a distance of 1000 km (10°), between heights of 1000-1500 m, the lower air mass was influenced by local air from SSW (at 300 m) and SW (500m) that had traveled during the last 24 h near the surface at heights up to 500 m over moderately polluted areas. Hence the lidar data show higher aerosol content in the lower layer (<500 m) than in the layer above (>600m) and both disconnected layers are from different origin.

This situation changed as indicated by the air mass trajectory arriving at 13:00 LT. The air mass arriving at 300 m had the same characteristics as at 10:00 LT, had traveled an even shorter distance and the layer adjacent to the surface was more stagnant. However, the air mass arriving at 500 m now came from the west, had traveled over clean areas (Fig 6a) at heights between 500 and 1000 m and thus was distinctly different from the layer below. The air mass arriving at 1000 m originated from a bit further north and further away (in Inner Mongolia) than at 10:00 LT, and had travelled at heights between 750 and 1000 m. Hence all three air masses suggest that the layers originated from different regions and likely had different composition.

The trajectories of the air masses arriving at 16:00 LT indicate that the situation had changed, i.e. the pollution episode was finished and pollution was replaced with cleaner air transported from the W to WNW over distances of hundreds of km and originating from elevations of 500-1000 m for air masses arriving at 300m and 500m, whereas the air mass arriving at 1000 m had actually followed a lower trajectory.
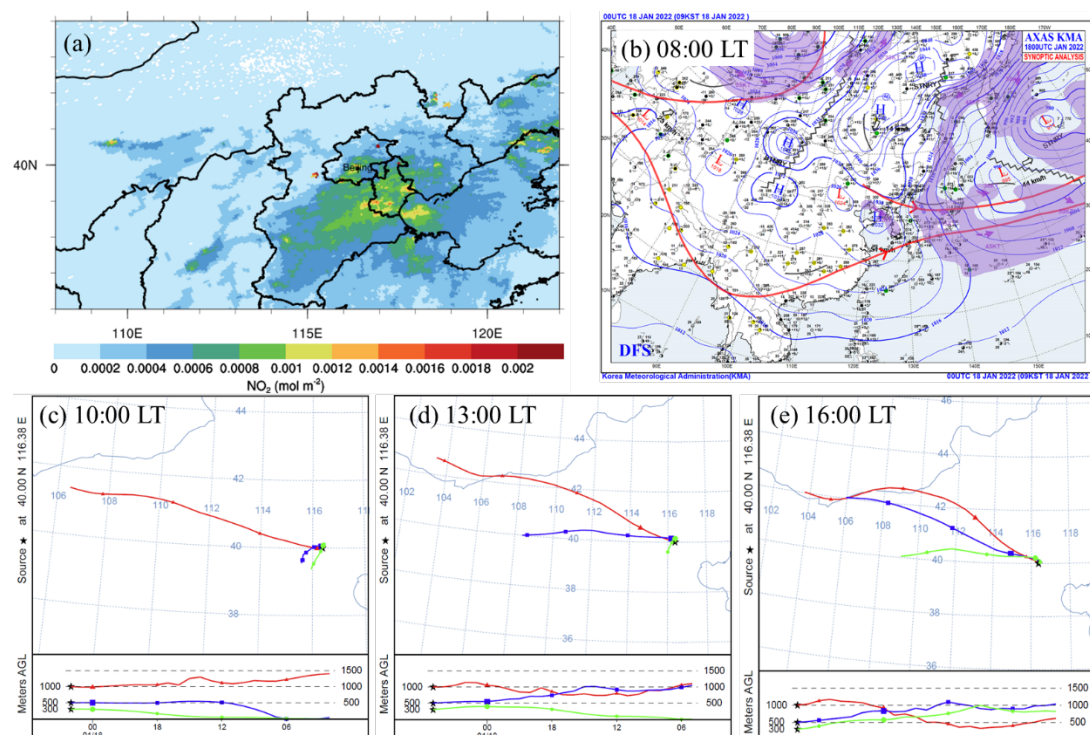
Figure 6. Same as Fig. 4, but for 18 January, 2022.

A comparative analysis of the two cases reveals distinct characteristics. Case 1, on January 14th, is characterized by a belt-shaped pollution event. The air mass arriving at 1000 m was primarily transported from Shanxi to Beijing arriving from the SW during the last 15 hours (Fig. 4c), while at lower levels the air masses travelled at low altitudes (from near the surface to 500 m) through the polluted area in Hebei (compare Figs. 4 a and c). In contrast, Case 2, on January 18th, was a large-scale pollution event covering Shandong, Hebei, and Henan and the southern part of Beijing (Fig. 6a), but the air mass arriving at 1000 m had been transported from the WNW over a large distance over clean areas. However, at lower levels, the air was stagnant (wind speed was low) in the morning, air masses arriving at 300 and 500 m at 10:00 LT had travelled over very short distances during the last 24 hours and were thus only influenced by local pollution. In Case 1, elevated pollutant concentrations were recorded in the 800-1000 m altitude layer in the morning, attributable to an air mass originating from Shanxi Province (with no significant pollution observed there) that was transported over the polluted area in Hebei at about 1000 m (Fig 4a and 4c), and then the upper-level air mass likely carried pollutant residuals which had been uplifted through vertical mixing processes over the

27

661 polluted area in Hebei. These pollutants were subsequently advected to Beijing, where

662 their presence was detected by lidar observations. Conversely, in Case 2, pollutants

663 were predominantly transported from the plains, leading to a significant accumulation

664 of pollutants in the near-surface layer. After 13:00, in both cases the distinction between

665 the pollutant layers disappeared when the boundary layers developed under the

666 influence of surface heating and increasing wind speed (Fig. 2), thus creating boundary

667 layer turbulence and mixing of NO_2, aerosols and other constituents. Both the total

668 VCD and NS concentrations of NO_2 increased, with that of total VCD of NO_2 being

669 more significant. This further suggests that it is more difficult to obtain NS NO_2

670 concentrations using total VCD of NO_2 concentrations during the morning hours.

671 However, utilizing the types of pollution spatial distribution and transport patterns can

672 be helpful in indicating NS NO_2 concentrations.

673 **3.3 Ratio of total VCD vs NS NO_2**

674   The two pollution cases discussed above show that the ratio between total VCD

675 and NS concentrations of NO_2 in the morning (before 13:00) is different from that in

676 the afternoon (after 13:00) during the study period in the winter in Beijing. In order to

677 better understand the relationship between total VCD and NS concentrations of NO_2,

678 we calculated their ratio for each day, while we also differentiated between the morning

679 and afternoon using 13:00 as the split time. The Ratio, defined as the ratio of total VCD

680 to NS NO_2 concentrations, serves a dual purpose: it not only quantifies the changes

681 between total VCD and NS concentrations of NO_2 when the correlation is low but also

682 reflects the degree of dispersion between the two measurements. A more variable Ratio

683 indicates higher dispersion and poorer correlation, providing a straightforward yet

684 effective way to assess the reliability of using total VCD of NO_2 to predict NS NO_2

685 concentrations.

686   The results are presented as violin plots in Fig. 7, for each of the 12 days for which

687 data are available. The data in fig. 7 show that the mean and median values of the NO_2

688 ratio during Period I (10-18 January were substantially higher than those during Period

689 III (25-30 January), with the exception of 25 and 29 January. During these two days, at

the beginning and end of Period III, signify the transition from polluted to clean days

(see fig. 2b). On most days the ratio was smaller in the morning than in the afternoon.

The difference between the morning and afternoon ratios was small during the two days

(14th and 18th) with accumulated pollution, while during the four days when wind speed

increased, on 13, 15, and 17, the differences were relatively large, with the largest

difference of 192 m on the 13th. During Period III the difference between the morning

and afternoon ratio was basically smaller than 50 m, with a gap of more than 100 m

only on the 29th. There were no valid observations of total VCD of NO_2 during Period

II, so it is not possible to judge the changes in ratio over multiple consecutive days of

pollution. Throughout the observation period, the standard deviations of the ratio were

overall larger in the morning than in the afternoon, when the winter boundary layer was

well-mixed and the relationship between total VCD and NS concentrations of NO_2 was

relatively stable. However, in the morning, when the boundary layer was developing,

the day-to-day variations in the standard deviation imply relatively large changes in the

ratio. The box plot in fig. 7b illustrates the difference between the morning and

afternoon ratios. The mean values are lower in the morning (364m) than in the afternoon

(428m), and the upper quartile in the afternoon are closer to their median value,

suggesting that the ratio is more stable in the afternoon when it is well mixed vertically.

However, although the ratio is quite stable in the afternoon when the boundary layer is

generally well mixed, there are still unpredictable extreme values (e.g. 771 m).

Generally, the temporal stability of the Ratio is important. The Ratio is overall less

variable after 13:00, suggesting that polar-orbiting satellites can be used to predict NS

NO_2 based on total VCD of NO_2 during this period with greater confidence. This

temporal stability is particularly valuable because it offers a feasible approach for air

quality monitoring and forecasting. In contrast, the Ratio is less stable before 13:00,

posing greater challenges for using geostationary satellites for the same prediction task.

It's worth noting that our analysis in winter in Beijing suggests that considering both

the spatial distribution of pollutants and their transport direction has the potential to

enhance the ability of satellites to predict NS NO_2 concentrations based on total VCD

719   of NO$_2$. By incorporating this information into prediction models, the accuracy and

720   reliability of satellite-based air quality predictions may be improved, particularly in

721   complex urban environments where pollutant concentrations can vary significantly

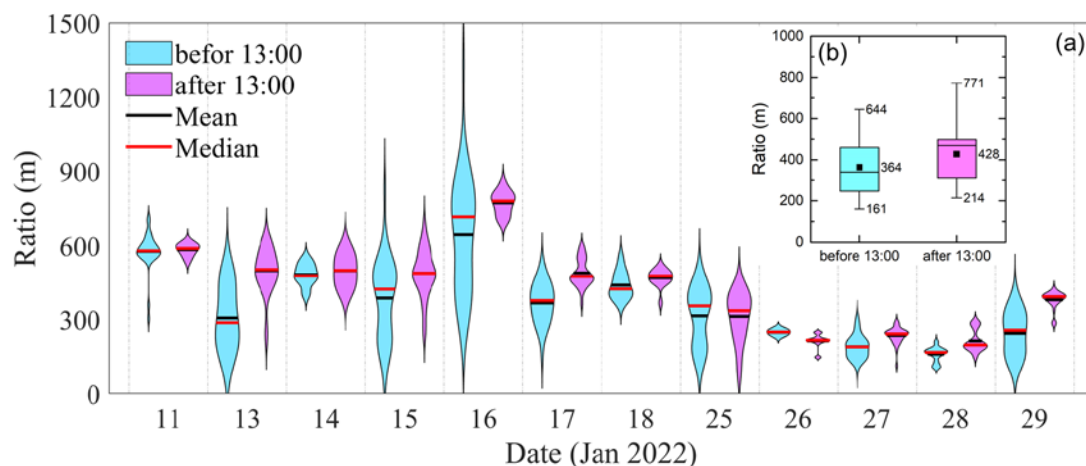722   over short distances and time periods.

723

724

725   **Figure 7**. (a) Violin plots of Ratio of total VCD and NS concentrations of NO$_2$ for each

726   day when observations were available in January 2022, where the data were

727   differentiated between morning (before 13:00 LT) and afternoon (after 13:00LT). (b)

728   The box-whisker plot of Ratio averaged over all observations before and after 13:00 in

729   January 2022. The horizontal lines in the boxes and the top and bottom edges represent

730   the mean and upper and lower quartile values of the Ratio, the solid square dots

731   represent the median values, and the bars represent the minimum and maximum values.

732   **4 Discussion and Conclusions**

733   Total column and near surface NO$_2$ data observed during the winter field experiment

734   from Jan 10 to Jan 29, 2022, at the Beijing RADI site were analyzed together with lidar,

735   PM$_{2.5}$ and meteorological data, satellite data, weather maps and air mass trajectories.

736   Based on these observations, the experimental period was sub-dived into three periods:

737   intermittent pollution days, persistent pollution days and clean days. The analysis of the

738   total VCD and NS concentrations of NO$_2$ shows substantial differences between the

739   first and third period, while during the second period with persistent pollution no total

740   VCD of NO$_2$ observations were available due to the presence of clouds. During the first

period, two episodes with high pollution were identified and analyzed in detail with a focus on the ratio between the variation of the total VCD and NS concentrations of NO_2 and their ratio. The relations between the total VCD and NS concentrations of NO_2 in the morning and in the afternoon, split at 13:00 LT, appear to be significantly different. These differences have been explained in terms of boundary layer dynamics, using lidar data showing the vertical stratification with disconnected boundary layers at different heights in the morning which connected as the boundary layer developed in the afternoon. In addition, the 4-layer NO_2 column concentrations obtained from Pandora show good agreement with the lidar signal in terms of the temporal and vertical variations of the NO_2 concentrations, with differences attributed to the different vertical resolutions of the Pandora and lidar observations, as well as physical properties of NO_2 and aerosols. From this, together with air mass trajectories, weather maps and TROPOMI satellite observations of the NO_2 spatial distribution, a consistent picture was created showing different source regions for disconnected airmasses arriving at different heights and different times of the day.

Data from the full experimental period, with 12 days for which valid data are available, were analyzed in detail to obtain more insight into the variation of the ratio between the total VCD and NS concentrations of NO_2. This ratio appears to be overall smaller in the morning than in the afternoon, with larger standard deviations. In addition, the ratios and their standard deviations were overall larger during the more polluted episode I than during the relatively clean period III.

Day-time continuous remote sensing observations of Pandora were used in this study and the results confirm its possible importance in understanding changes in the distribution of NO_2 in the vertical direction. The NO_2 vertical distribution has been analyzed using less than 3 weeks of observation data, which has some limitations, but the research idea is worthy of reference and promotion. In the future, the implementation of larger-scale experiments in different typical regions and seasons will help to provide further understanding of the ideas presented in this study and improve the shortcomings. Moreover, we will broaden the scope of experimental areas and field

sites to complement research on the various pollutant emission and transport characteristics. Furthermore, observations over a longer period will allow us to capture more representative cases, thereby enhancing the reliability of our findings.

The overall conclusion from this study during a relatively short period of almost 3 weeks in the winter in Beijing is that the variation between the total column and near surface NO_2 concentrations varies with the concentration level and the time of day. In the afternoon the boundary layer is well developed and satellite observations are sensitive to the NS concentrations, whereas in the morning this depends on meteorological conditions. Hence, satellites with an afternoon overpass are capable to measure total VCD of NO_2 which is representative for NS concentrations, whereas observations earlier in the day may not be. This could possibly affect the interpretation of diurnal variations derived from observations using geostationary satellite.

References

Atkinson, R.: Atmospheric chemistry of VOCs and NO$_x$, Atmospheric Environment, 34, 2063-2101, https://doi.org/10.1016/S1352-2310(99)00460-4, 2000.

BAM 1020 particulate monitor operation manual (2020), Met One Instuments, Inc. https://metone.com/wp-content/uploads/2020/09/BAM-1020-9805-Manual-Rev-C.pdf.

Boersma, K. F., Jacob, D. J., Trainic, M., Rudich, Y., DeSmedt, I., Dirksen, R., and Eskes, H. J.: Validation of urban NO$_2$ concentrations and their diurnal and seasonal variations observed from the SCIAMACHY and OMI sensors using in situ surface measurements in Israeli cities, Atmos. Chem. Phys., 9, 3867-3879, 10.5194/acp-9-3867-2009, 2009.

Burrows, J. P., Weber, M., Buchwitz, M., Rozanov, V., Ladstätter-Weißenmayer, A., Richter, A., DeBeek, R., Hoogen, R., Bramstedt, K., Eichmann, K.-U., Eisinger, M., and Perner, D.: The Global Ozone Monitoring Experiment (GOME): Mission Concept and First Scientific Results, Journal of the Atmospheric Sciences, 56, 151-175, https://doi.org/10.1175/1520-0469(1999)056<0151:TGOMEG>2.0.CO;2, 1999.

Chang, B., Liu, H., Zhang, C., Xing, C., Tan, W., and Liu, C.: Relating satellite NO2 tropospheric columns to near-surface concentrations: implications from ground-based MAX-DOAS NO2 vertical profile observations, npj Climate and Atmospheric Science, 8, 1, 10.1038/s41612-024-00891-z, 2025.

Chang, L. S., Kim, D., Hong, H., Kim, D. R., Yu, J. A., Lee, K., Lee, H., Kim, D., Hong, J., Jo, H. Y., and Kim, C. H.: Evaluation of correlated Pandora column NO2 and in situ surface NO2 measurements during GMAP campaign, Atmos. Chem. Phys., 22, 10703-10720, 10.5194/acp-22-10703-2022, 2022.

Chang, X., Wang, S., Zhao, B., Xing, J., Liu, X., Wei, L., Song, Y., Wu, W., Cai, S., Zheng, H., Ding, D., and Zheng, M.: Contributions of inter-city and regional transport to PM2.5 concentrations in the Beijing-Tianjin-Hebei region and its implications on regional joint air pollution control, Science of The Total Environment, 660, 1191-1200, https://doi.org/10.1016/j.scitotenv.2018.12.474, 2019.

Cede, A. (2024). Manual for Blick Software Suite 1.8; Manual version 1.8-5, 14 Aug 2024 (202 pp.) available from https://www.pandonia-global-network.org/wp-content/uploads/2024/08/BlickSoftwareSuite_Manual_v1-8-5.pdf (last visited 21 January, 2025)

Chen, Z.-Y., Zhang, T.-H., Zhang, R., Zhu, Z.-M., Yang, J., Chen, P.-Y., Ou, C.-Q., and Guo, Y.: Extreme gradient boosting model to estimate PM$_{2.5}$ concentrations with missing-filled satellite data in China, Atmospheric Environment, 202, 180-189, https://doi.org/10.1016/j.atmosenv.2019.01.027, 2019.

Cheng, N., Li, Y., Sun, F., Chen, C., Wang, B., Li, Q., Wei, P., and Cheng, B.: Ground-Level NO$_2$ in Urban Beijing: Trends, Distribution, and Effects of Emission Reduction Measures, Aerosol and Air Quality Research, 18, 343-356, 10.4209/aaqr.2017.02.0092, 2018.

de Leeuw, G., van der A, R., Bai, J., Xue, Y., Varotsos, C., Li, Z., Fan, C., Chen, X., Christodoulakis, I., Ding, J., Hou, X., Kouremadas, G., Li, D., Wang, J., Zara, M., Zhang, K., and Zhang, Y.: Air Quality over China, 10.3390/rs13173542, 2021.

de Souza, A., Aristone, F., Abreu, M. C., de Oliveira-Júnior, J. F., Fernandes, W. A., and Pobocikova, I.: Spatio-temporal variations of tropospheric nitrogen dioxide in South Mato Grosso based on remote sensing by satellite, Meteorology and Atmospheric Physics, 134, 19, 10.1007/s00703-021-00855-5, 2022.

Ding, J., van der A, R. J., Mijling, B., Jalkanen, J.-P., Johansson, L., and Levelt, P. F.: Maritime NOx Emissions Over Chinese Seas Derived From Satellite Observations, Geophysical Research Letters, 45, 2031-2037, https://doi.org/10.1002/2017GL076788, 2018.

Dong, Z., Wang, S., Xing, J., Chang, X., Ding, D., and Zheng, H.: Regional transport in Beijing-Tianjin-Hebei region and its changes during 2014–2017: The impacts of meteorology and emission reduction, Science of The Total Environment, 737, 139792, https://doi.org/10.1016/j.scitotenv.2020.139792, 2020.

Dou, X., Liao, C., Wang, H., Huang, Y., Tu, Y., Huang, X., Peng, Y., Zhu, B., Tan, J., Deng, Z., Wu, N., Sun, T., Ke, P., and Liu, Z.: Estimates of daily ground-level NO_2 concentrations in China based on Random Forest model integrated K-means, Advances in Applied Energy, 2, 100017, https://doi.org/10.1016/j.adapen.2021.100017, 2021.

Draxler, R. R.: An Overview of the HYSPLIT_4 Modelling System for Trajectories, Dispersion, and Deposition, https://www.arl.noaa.gov/documents/reports/MetMag.pdf, 1998.

Duncan, B. N., Lamsal, L. N., Thompson, A. M., Yoshida, Y., Lu, Z., Streets, D. G., Hurwitz, M. M., and Pickering, K. E.: A space-based, high-resolution view of notable changes in urban NOx pollution around the world (2005–2014), Journal of Geophysical Research: Atmospheres, 121, 976-996, https://doi.org/10.1002/2015JD024121, 2016.

Eum, K.-D., Kazemiparkouhi, F., Wang, B., Manjourides, J., Pun, V., Pavlu, V., and Suh, H.: Long-term NO2 exposures and cause-specific mortality in American older adults, Environment International, 124, 10-15, https://doi.org/10.1016/j.envint.2018.12.060, 2019.

Eum, K.-D., Honda, T. J., Wang, B., Kazemiparkouhi, F., Manjourides, J., Pun, V. C., Pavlu, V., and Suh, H.: Long-term nitrogen dioxide exposure and cause-specific mortality in the U.S. Medicare population, Environmental Research, 207, 112154, https://doi.org/10.1016/j.envres.2021.112154, 2022.

Fan, C., Li, Z., Li, Y., Dong, J., van der A, R., and de Leeuw, G.: Variability of NO2 concentrations over China and effect on air quality derived from satellite and ground-based observations, Atmos. Chem. Phys., 21, 7723-7748, 10.5194/acp-21-7723-2021, 2021.

Flynn, C. M., Pickering, K. E., Crawford, J. H., Lamsal, L., Krotkov, N., Herman, J., Weinheimer, A., Chen, G., Liu, X., Szykman, J., Tsay, S.-C., Loughner, C., Hains,

J., Lee, P., Dickerson, R. R., Stehr, J. W., and Brent, L.: Relationship between column-density and surface mixing ratio: Statistical analysis of O_3 and NO_2 data from the July 2011 Maryland DISCOVER-AQ mission, Atmospheric Environment, 92, 429-441, https://doi.org/10.1016/j.atmosenv.2014.04.041, 2014.

Goldberg, D. L., Anenberg, S. C., Kerr, G. H., Mohegh, A., Lu, Z., and Streets, D. G.: TROPOMI NO2 in the United States: A Detailed Look at the Annual Averages, Weekly Cycles, Effects of Temperature, and Correlation With Surface NO_2 Concentrations, Earth's Future, 9, e2020EF001665, https://doi.org/10.1029/2020EF001665, 2021.

Herman, J., Cede, A., Spinei, E., Mount, G., Tzortziou, M., and Abuhassan, N.: NO2 column amounts from ground-based Pandora and MFDOAS spectrometers using the direct-sun DOAS technique: Intercomparisons and application to OMI validation, Journal of Geophysical Research: Atmospheres, 114, https://doi.org/10.1029/2009JD011848, 2009.

Herman, J., Abuhassan, N., Kim, J., Kim, J., Dubey, M., Raponi, M., and Tzortziou, M.: Underestimation of column NO_2 amounts from the OMI satellite compared to diurnally varying ground-based retrievals from multiple PANDORA spectrometer instruments, Atmos. Meas. Tech., 12, 5593-5612, 10.5194/amt-12-5593-2019, 2019.

Huang, X., Yang, K., Kondragunta, S., Wei, Z., Valin, L., Szykman, J., and Goldberg, M.: NO_2 retrievals from NOAA-20 OMPS: Algorithm, evaluation, and observations of drastic changes during COVID-19, Atmospheric Environment, 290, 119367, https://doi.org/10.1016/j.atmosenv.2022.119367, 2022.

Ialongo, I., Virta, H., Eskes, H., Hovila, J., and Douros, J.: Comparison of TROPOMI/Sentinel-5 Precursor NO_2 observations with ground-based measurements in Helsinki, Atmos. Meas. Tech., 13, 205-218, 10.5194/amt-13-205-2020, 2020.

Jiang, L., Chen, Y., Zhou, H., and He, S.: NO_x emissions in China: Temporal variations, spatial patterns and reduction potentials, Atmospheric Pollution Research, 11, 1473-1480, https://doi.org/10.1016/j.apr.2020.06.003, 2020.

Kang, Y., Tang, G., Li, Q., Liu, B., Cao, J., Hu, Q., and Wang, Y.: Evaluation and Evolution of MAX-DOAS-observed Vertical NO2 Profiles in Urban Beijing, Advances in Atmospheric Sciences, 38, 1188-1196, 10.1007/s00376-021-0370-1, 2021.

Kim, J., Jeong, U., Ahn, M.-H. et al.: New Era of Air Quality Monitoring from Space: Geostationary Environment Monitoring Spectrometer (GEMS), Bulletin of the American Meteorological Society, 101, E1-E22, https://doi.org/10.1175/BAMS-D-18-0013.1, 2020.

Knepp, T., Pippin, M., Crawford, J., Chen, G., Szykman, J., Long, R., Cowen, L., Cede, A., Abuhassan, N., Herman, J., Delgado, R., Compton, J., Berkoff, T., Fishman, J., Martins, D., Stauffer, R., Thompson, A. M., Weinheimer, A., Knapp, D., Montzka, D., Lenschow, D., and Neil, D.: Estimating surface NO_2 and SO_2 mixing ratios from fast-response total column observations and potential application to geostationary missions, Journal of Atmospheric Chemistry, 72, 261-286,

10.1007/s10874-013-9257-6, 2015.

KNMI (2017), Algorithm theoretical basis document for the TROPOMI L01b data processor, Tech. Rep. S5P-KNMI-L01B 0009-SD, Koninklijk Nederlands Meteorologisch Instituut (KNMI), CI-6480-ATBD, issue 8.0.0, available at: https://sentinels.copernicus.eu/documents/247904/2476257/Sentinel-5P-TROPOMI-Level-1B-ATBD (last access: 11 January 2020).

Kornartit, C., Sokhi, R. S., Burton, M. A., and Ravindra, K.: Activity pattern and personal exposure to nitrogen dioxide in indoor and outdoor microenvironments, Environment International, 36, 36-45, https://doi.org/10.1016/j.envint.2009.09.004, 2010.

Lamsal, L. N., Krotkov, N. A., Celarier, E. A., Swartz, W. H., Pickering, K. E., Bucsela, E. J., Gleason, J. F., Martin, R. V., Philip, S., Irie, H., Cede, A., Herman, J., Weinheimer, A., Szykman, J. J., and Knepp, T. N.: Evaluation of OMI operational standard NO_2 column retrievals using in situ and surface-based NO_2 observations, Atmos. Chem. Phys., 14, 11587-11609, 10.5194/acp-14-11587-2014, 2014.

Levelt, P. F., Oord, G. H. J. v. d., Dobber, M. R., Malkki, A., Huib, V., Johan de, V., Stammes, P., Lundell, J. O. V., and Saari, H.: The ozone monitoring instrument, IEEE Transactions on Geoscience and Remote Sensing, 44, 1093-1101, 10.1109/TGRS.2006.872333, 2006.

Li, D., Liu, J., Zhang, J., Gui, H., Du, P., Yu, T., Wang, J., Lu, Y., Liu, W., and Cheng, Y.: Identification of long-range transport pathways and potential sources of PM2.5 and PM10 in Beijing from 2014 to 2015, Journal of Environmental Sciences, 56, 214-229, https://doi.org/10.1016/j.jes.2016.06.035, 2017.

Li, J., Wang, Y., Zhang, R., Smeltzer, C., Weinheimer, A., Herman, J., Boersma, K. F., Celarier, E. A., Long, R. W., Szykman, J. J., Delgado, R., Thompson, A. M., Knepp, T. N., Lamsal, L. N., Janz, S. J., Kowalewski, M. G., Liu, X., and Nowlan, C. R.: Comprehensive evaluations of diurnal NO_2 measurements during DISCOVER-AQ 2011: effects of resolution-dependent representation of NO_x emissions, Atmos. Chem. Phys., 21, 11133-11160, 10.5194/acp-21-11133-2021, 2021.

Liu, O., Li, Z., Lin, Y., Fan, C., Zhang, Y., Li, K., Zhang, P., Wei, Y., Chen, T., Dong, J., and de Leeuw, G.: Evaluation of the first year of Pandora NO_2 measurements over Beijing and application to satellite validation, Atmos. Meas. Tech., 17, 377-395, 10.5194/amt-17-377-2024, 2024.

Model 42i Trace Level Manual (2007). https://cires1.colorado.edu/jimenez-group/Manuals/Manual_NOx_42i.pdf.

Nordeide Kuiper, I., Svanes, C., Markevych, I., Accordini, S., Bertelsen, R. J., Bråbäck, L., Heile Christensen, J., Forsberg, B., Halvorsen, T., Heinrich, J., Hertel, O., Hoek, G., Holm, M., de Hoogh, K., Janson, C., Malinovschi, A., Marcon, A., Miodini Nilsen, R., Sigsgaard, T., and Johannessen, A.: Lifelong exposure to air pollution and greenness in relation to asthma, rhinitis and lung function in adulthood, Environment International, 146, 106219, https://doi.org/10.1016/j.envint.2020.106219, 2021.

Qin, K., Rao, L., Xu, J., Bai, Y., Zou, J., Hao, N., Li, S., and Yu, C.: Estimating Ground Level NO_2 Concentrations over Central-Eastern China Using a Satellite-Based

Geographically and Temporally Weighted Regression Model, 10.3390/rs9090950, 2017.

Qin, K., Han, X., Li, D., Xu, J., Loyola, D., Xue, Y., Zhou, X., Li, D., Zhang, K., and Yuan, L.: Satellite-based estimation of surface NO_2 concentrations over east-central China: A comparison of POMINO and OMNO2d data, Atmospheric Environment, 224, 117322, https://doi.org/10.1016/j.atmosenv.2020.117322, 2020.

Reed, A. J., Thompson, A. M., Kollonige, D. E., Martins, D. K., Tzortziou, M. A., Herman, J. R., Berkoff, T. A., Abuhassan, N. K., and Cede, A.: Effects of local meteorology and aerosols on ozone and nitrogen dioxide retrievals from OMI and pandora spectrometers in Maryland, USA during DISCOVER-AQ 2011, Journal of Atmospheric Chemistry, 72, 455-482, 10.1007/s10874-013-9254-9, 2015.

Sandradewi, J., Prévôt, A. S. H., Szidat, S., Perron, N., Alfarra, M. R., Lanz, V. A., Weingartner, E., and Baltensperger, U.: Using aerosol light absorption measurements for the quantitative determination of wood burning and traffic emission contributions to particulate matter, Environmental science & technology, 42 9, 3316-3323, 2008.

Scientific, M. (2016). Aethalometer Model AE33 User Manual, version 1.54. Aerosol doo, Ljubljana, Slovenia. https://gml.noaa.gov/aftp/aerosol/doc/manuals/AE33_UsersManual_Rev154.pdf.

Song, J., Zang, L., Mao, F., Zhang, Y., and Chen, J.: Hourly near-ground NO2 concentration retrieval from geostationary satellite observations, Int. Arch. Photogramm. Remote Sens. Spatial Inf. Sci., XLVIII-1-2024, 599-604, 10.5194/isprs-archives-XLVIII-1-2024-599-2024, 2024.

Sorek-Hamer, M., Strawa, A. W., Chatfield, R. B., Esswein, R., Cohen, A., and Broday, D. M.: Improved retrieval of PM2.5 from satellite data products using non-linear methods, Environmental Pollution, 182, 417-423, https://doi.org/10.1016/j.envpol.2013.08.002, 2013.

Stein, A. F., Draxler, R. R., Rolph, G. D., Stunder, B. J. B., Cohen, M. D., and Ngan, F.: NOAA's HYSPLIT Atmospheric Transport and Dispersion Modeling System, Bulletin of the American Meteorological Society, 96, 2059-2077, https://doi.org/10.1175/BAMS-D-14-00110.1, 2015.

Stull, R.B.: An Introduction to Boundary Layer Meteorology. Kluwer Academic Publishers, Dordrecht, The Netherlands. (666 pp.). ISBN 90-227-2768-6. https://doi.org/10.1007/978-94-009-3027-8, 1988.

Sun, T., Zhang, T., Xiang, Y., Fan, G., Fu, Y., and Lv, L.: Investigation on the vertical distribution and transportation of PM2.5 in the Beijing-Tianjin-Hebei region based on stereoscopic observation network, Atmospheric Environment, 294, 119511, https://doi.org/10.1016/j.atmosenv.2022.119511, 2023.

Tang, T., Cheng, T., Zhu, H., Ye, X., Fan, D., Li, X., and Tong, H.: Quantifying instantaneous nitrogen oxides emissions from power plants based on space observations, Science of The Total Environment, 938, 173479, https://doi.org/10.1016/j.scitotenv.2024.173479, 2024.

Thompson, A. M., Stauffer, R. M., Boyle, T. P., Kollonige, D. E., Miyazaki, K.,

Tzortziou, M., Herman, J. R., Abuhassan, N., Jordan, C. E., and Lamb, B. T.: Comparison of Near-Surface NO2 Pollution With Pandora Total Column NO2 During the Korea-United States Ocean Color (KORUS OC) Campaign, Journal of Geophysical Research: Atmospheres, 124, 13560-13575, https://doi.org/10.1029/2019JD030765, 2019.

Tzortziou, M., Herman, J. R., Cede, A., Loughner, C. P., Abuhassan, N., and Naik, S.: Spatial and temporal variability of ozone and nitrogen dioxide over a major urban estuarine ecosystem, Journal of Atmospheric Chemistry, 72, 287-309, 10.1007/s10874-013-9255-8, 2015.

Tzortziou, M., Parker, O., Lamb, B., Herman, J. R., Lamsal, L., Stauffer, R., and Abuhassan, N.: Atmospheric Trace Gas (NO_2 and O_3) Variability in South Korean Coastal Waters, and Implications for Remote Sensing of Coastal Ocean Color Dynamics, 10.3390/rs10101587, 2018.

van der A, R. J., Peters, D. H. M. U., Eskes, H., Boersma, K. F., Van Roozendael, M., De Smedt, I., and Kelder, H. M.: Detection of the trend and seasonal variation in tropospheric NO_2 over China, Journal of Geophysical Research: Atmospheres, 111, https://doi.org/10.1029/2005JD006594, 2006.

van der A, R. J., Mijling, B., Ding, J., Koukouli, M. E., Liu, F., Li, Q., Mao, H., and Theys, N.: Cleaning up the air: effectiveness of air quality policy for SO_2 and NO_x emissions in China, Atmos. Chem. Phys., 17, 1775-1789, 10.5194/acp-17-1775-2017, 2017.

van Geffen, J. H. G. M., Eskes, H. J., Boersma, K. F., Maasakkers, J. D., and Veefkind, J. P. (2019), TROPOMI ATBD of the total and tropospheric NO_2 data products, Tech. Rep. S5P-KNMI-L2-0005-RP, Koninklijk Nederlands Meteorologisch Instituut (KNMI), CI-7430-ATBD, issue 1.4.0, available at: https://sentinels.copernicus.eu/documents/247904/2476257/Sentinel-5P-TROPOMI-ATBD-NO2-data-products (last access: 11 January 2020).

van Geffen, J. H. G. M., Boersma, K. F., Van Roozendael, M., Hendrick, F., Mahieu, E., De Smedt, I., Sneep, M., and Veefkind, J. P.: Improved spectral fitting of nitrogen dioxide from OMI in the 405–465 nm window, Atmos. Meas. Tech., 8, 1685-1699, 10.5194/amt-8-1685-2015, 2015.

Veefkind, J. P., Aben, I., McMullan, K., Förster, H., de Vries, J., Otter, G., Claas, J., Eskes, H. J., de Haan, J. F., Kleipool, Q., van Weele, M., Hasekamp, O., Hoogeveen, R., Landgraf, J., Snel, R., Tol, P., Ingmann, P., Voors, R., Kruizinga, B., Vink, R., Visser, H., and Levelt, P. F.: TROPOMI on the ESA Sentinel-5 Precursor: A GMES mission for global observations of the atmospheric composition for climate, air quality and ozone layer applications, Remote Sensing of Environment, 120, 70-83, https://doi.org/10.1016/j.rse.2011.09.027, 2012.

Wang, Y., Dörner, S., Donner, S., Böhnke, S., De Smedt, I., Dickerson, R. R., Dong, Z., He, H., Li, Z., Li, Z., Li, D., Liu, D., Ren, X., Theys, N., Wang, Y., Wang, Y., Wang, Z., Xu, H., Xu, J., and Wagner, T.: Vertical profiles of NO2, SO2, HONO, HCHO, CHOCHO and aerosols derived from MAX-DOAS measurements at a rural site in the central western North China Plain and their relation to emission sources and effects of regional transport, Atmos. Chem. Phys., 19, 5417-5449, 10.5194/acp-

19-5417-2019, 2019.

Wei, J., Liu, S., Li, Z., Liu, C., Qin, K., Liu, X., Pinker, R. T., Dickerson, R. R., Lin, J., Boersma, K. F., Sun, L., Li, R., Xue, W., Cui, Y., Zhang, C., and Wang, J.: Ground-Level NO_2 Surveillance from Space Across China for High Resolution Using Interpretable Spatiotemporally Weighted Artificial Intelligence, Environmental Science & Technology, 56, 9988-9998, 10.1021/acs.est.2c03834, 2022.

Xing, C., Liu, C., Wang, S., Chan, K. L., Gao, Y., Huang, X., Su, W., Zhang, C., Dong, Y., Fan, G., Zhang, T., Chen, Z., Hu, Q., Su, H., Xie, Z., and Liu, J.: Observations of the vertical distributions of summertime atmospheric pollutants and the corresponding ozone production in Shanghai, China, Atmos. Chem. Phys., 17, 14275-14289, 10.5194/acp-17-14275-2017, 2017.

Yin, D., Song, Q., Guo, Y., Jiang, Y., Dong, Z., Zhao, B., Wang, S., Gao, D., Chang, X., Zheng, H., Li, S., Li, Y., and Liu, B.: Regional transport characteristics of $PM_{2.5}$ pollution events in Beijing during 2018–2021, Journal of Environmental Sciences, 152, 503-515, https://doi.org/10.1016/j.jes.2024.05.044, 2025.

Zhang, C., Liu, C., Li, B., Zhao, F., and Zhao, C.: Spatiotemporal neural network for estimating surface NO2 concentrations over north China and their human health impact, Environmental Pollution, 307, 119510, https://doi.org/10.1016/j.envpol.2022.119510, 2022.

Zhang, T., Zhang, R., Zhong, J., Che, H., Wang, J., and Guo, L.: The vertical pollution structure reflected by aerosol optical properties in Beijing and its relation with meteorological conditions in the autumn and winter of 2017–2020, Atmospheric Environment, 308, 119870, https://doi.org/10.1016/j.atmosenv.2023.119870, 2023.

Zhang, Y., Wang, Y., Chen, G., Smeltzer, C., Crawford, J., Olson, J., Szykman, J., Weinheimer, A. J., Knapp, D. J., Montzka, D. D., Wisthaler, A., Mikoviny, T., Fried, A., and Diskin, G.: Large vertical gradient of reactive nitrogen oxides in the boundary layer: Modeling analysis of DISCOVER-AQ 2011 observations, Journal of Geophysical Research: Atmospheres, 121, 1922-1934, https://doi.org/10.1002/2015JD024203, 2016.

Zhao, R., Gu, X., Xue, B., Zhang, J., and Ren, W.: Short period PM2.5 prediction based on multivariate linear regression model, PLOS ONE, 13, e0201011, 10.1371/journal.pone.0201011, 2018.

Zhao, Z., Lu, Y., Zhan, Y., Cheng, Y., Yang, F., Brook, J. R., and He, K.: Long-term spatiotemporal variations in surface NO_2 for Beijing reconstructed from surface data and satellite retrievals, Science of The Total Environment, 904, 166693, https://doi.org/10.1016/j.scitotenv.2023.166693, 2023.

Zhao, X., Griffin, D., Fioletov, V., McLinden, C., Cede, A., Tiefengraber, M., Müller, M., Bognar, K., Strong, K., Boersma, F., Eskes, H., Davies, J., Ogyu, A., and Lee, S. C.: Assessment of the quality of TROPOMI high-spatial-resolution NO_2 data products in the Greater Toronto Area, Atmos. Meas. Tech., 13, 2131-2159, 10.5194/amt-13-2131-2020, 2020.

1102
1103

1104